



An RBF-based finite difference discretization of the Navier-Stokes equations: error analysis and application to lid-driven cavity flows

Tianyi Chu* and Oliver T. Schmidt†
University of California San Diego, La Jolla, California 92093

Radial basis function-finite differences (RBF-FD) are used to solve the incompressible Navier-Stokes equations on scattered nodes. We present a semi-implicit fractional-step method that uses a staggered grid arrangement. The RBF-QR method devised by Fornberg and Piret [1] is used to obtain the RBF-FD weights for the spatial derivatives. We propose a rigorous error analysis strategy to identify optimal combinations of the shape parameter, ϵ , and the stencil size, n . A modified wavenumber analysis shows that the accuracy of the RBF differentiation matrices based on the optimal parameters is comparable to 4th-order Padé-type finite differences, for both first and second derivatives. The internal flow in a lid-driven cavity is studied as an example. We demonstrate that stable solutions are obtained without the need for hyperviscosity.

I. Nomenclature

α, β	=	grid indices
A, A_Ψ	=	interpolation matrices
$D_{\mathcal{L}}$	=	global RBF-based differentiation matrix
$\delta_{\mathcal{L}}$	=	local RBF-based differentiation matrix
ϵ	=	shape parameter
Δr	=	characteristic distance
Δt	=	time step
k	=	wavenumber
k^*	=	modified wavenumber
λ	=	RBF coefficient
\mathcal{L}	=	linear operator
m, n	=	local stencil size
M, N	=	total amount of nodes
p	=	pressure
$\phi(r), \psi(r)$	=	radial functions
Re	=	Reynolds number
u	=	horizontal velocity
v	=	vertical velocity
w	=	RBF weights
x	=	node location

II. Introduction

The radial basis functions (RBFs) method is a flexible tool to approximate functions on scattered nodes. A shape parameter describes the flatness of a smooth radial function and significantly impacts accuracy and numerical conditioning. The RBF methodology was originated from the idea of scattered data interpolation by Hardy [2]. The pioneering work by Powell [3] acknowledges that the interpolation matrices of Gaussian RBFs are nonsingular regardless of the shape parameters. The dependence of the interpolation error on the shape parameters is studied by Larsson and

*Ph.D. Student, Department of Mechanical and Aerospace Engineering. Student Member AIAA.

†Assistant Professor, Department of Mechanical and Aerospace Engineering. Member AIAA.

Fornberg [4] both theoretically and numerically. The idea of incorporating RBFs and the classical finite difference (FD) method was first proposed in a conference presentation by Tolstykh [5]. The so-called RBF-FD method generalizes the classical FD methods to arbitrary node layouts by approximating the desired function based on polyharmonic RBFs. Since good geometric flexibility and computational efficiency are achieved, the RBF-FD method is highly competitive to other high-order spectral methods and has been applied to solve partial differential equations (PDEs) on unstructured meshes. Flyer and Wright [6] studied the shallow water flows on a sphere based on the RBF-FD method and gave comparisons to other spectral element methods. Later, the numerical stability of this algorithm is improved by Flyer et al. [7] through the implementation of hyperviscosity [8]. When the radial function is nearly flat, the RBF discretizations suffer from the ill-conditioning of the interpolation matrices. To overcome this problem, Fornberg and Piret [1] proposed a numerically stable scheme for nodes on the surface of a sphere, which utilizes the QR-factorization to convert the original basis functions to a well-conditioned base. This so-called RBF-QR method is then generalized by Fornberg et al. [9] for arbitrary scattered nodes in up to three dimensions using Gaussian RBFs. As an extension, Larsson et al. [10] investigated the use of the RBF-QR approach for computing differentiation matrices and demonstrated the results by solving a two-dimensional Poisson's equation in an irregular domain. Fornberg and Flyer [11] summarized the procedure for solving PDEs with the RBF-based methods and presented different test cases, including the compressible Navier-Stokes equations. In this work, we implement the RBF-QR method to approximate the spatial derivatives based on an unstructured staggered grid, introduced next.

Staggered-grid avoids numerical instability from odd-even decoupling, a discretization error occurring on collocated grids, by arranging different variables at different locations. The choice of a staggered grid is natural for a finite volume method, where the flux is defined across the cell edge. Several finite volume methods with different staggering arrangements successfully solved incompressible Navier-Stokes equations on unstructured meshes in previous works. For example, Despotis and Tsangaris [12], Hwang [13, 14], Rida et al. [15] located the velocities at the middle of a cell's faces and pressure at the center of the cell with unstructured triangular meshes; Thomadakis and Leschziner [16] proposed an unstructured staggered grid with the velocity at the vertex of the cell and the pressure at the cell centroid; Shu et al. [17] switched the previous arrangement to have pressure at the vertex of cell and velocity at the cell centroid. We present a different staggering strategy in this work, which evaluates the pressure at the vertex of the cell and velocity at the cell interface. Rather than using the finite volume method, we take advantage of the RBF discretizations to compute differentiation matrices bases on the obtained scattered nodes.

Error analysis for RBF is not straightforward and is often done in a problem-specific manner. A large amount of works, most empirically, has been devoted to investigating optimal parameters for RBFs, including node arrangement, basis function, shape parameter, and stencil size (see e.g. [2, 18–22]). In this work, we propose a rigorous error analysis to optimize the RBF-QR method based on the idea of modified wavenumber known from classical finite difference [23], which is a measure of accuracy at different wavenumbers. The modified wavenumber analysis is widely used to examine the truncation error of different finite different methods and is also adapted for unstructured-grid schemes, see e.g. Park and Mahesh [24], Nishikawa [25]. Based on sinusoidal test functions, we establish the use of the nondimensionalized shape parameter and stencil size as appropriate parameterizations of the optimization. Furthermore, the accuracy of the optimal combinations is quantified by the modified wavenumber analysis on the unstructured staggered grid. Finally, the comparisons are made to well-established Padé type schemes.

This paper is organized as follows. §III gives a brief review of the RBF-QR method. §IV describes the generation of the unstructured staggered grid using the Matlab algorithm `DistMesh` [26]. §VI establishes the error analysis and the obtained optimal parameters. As an example, the lid-driven cavity problem is explored in §VII without implementing hyperviscosity. The results are compared to the benchmark data provided by Ghia et al. [27]. Finally, §VIII concludes and summarizes the paper.

III. Radial basis functions (RBFs)

The method of radial basis functions (RBFs) approximates a given function $f(\mathbf{x})$ using a set of smooth radial function $\phi(r)$. The idea of RBF is to seek the interpolant

$$s(\mathbf{x}) = \sum_{j=1}^n \lambda_j \phi(\|\mathbf{x} - \mathbf{x}_j\|) \quad (1)$$

such that $s(\mathbf{x}_i) = f(\mathbf{x}_i)$ for $i = 1, 2, \dots, n$, where $\{\mathbf{x}\}_{j=1}^n$ is a set of scattered nodes, and $\|\cdot\|$ denotes the standard Euclidean norm. Here, the local stencil size n can be different from the total number of grid points N . The interpolation

coefficients $\lambda_1, \dots, \lambda_n$ can be found by solving the linear system problem

$$\underbrace{\begin{bmatrix} \phi(\|\mathbf{x}_1 - \mathbf{x}_1\|) & \phi(\|\mathbf{x}_1 - \mathbf{x}_2\|) & \cdots & \phi(\|\mathbf{x}_1 - \mathbf{x}_n\|) \\ \phi(\|\mathbf{x}_2 - \mathbf{x}_1\|) & \phi(\|\mathbf{x}_2 - \mathbf{x}_2\|) & \cdots & \phi(\|\mathbf{x}_2 - \mathbf{x}_n\|) \\ \vdots & \vdots & \ddots & \vdots \\ \phi(\|\mathbf{x}_n - \mathbf{x}_1\|) & \phi(\|\mathbf{x}_n - \mathbf{x}_2\|) & \cdots & \phi(\|\mathbf{x}_n - \mathbf{x}_n\|) \end{bmatrix}}_{\mathbf{A}} \begin{bmatrix} \lambda_1 \\ \lambda_2 \\ \vdots \\ \lambda_n \end{bmatrix} = \begin{bmatrix} f(\mathbf{x}_1) \\ f(\mathbf{x}_2) \\ \vdots \\ f(\mathbf{x}_n) \end{bmatrix}, \quad (2)$$

where \mathbf{A} is the interpolation matrix. The obtained RBF interpolant $s(\mathbf{x})$ can then be used to approximate the given function function $f(\mathbf{x})$.

A. RBF-FD method

The use of RBFs can be applied to compute differentiation matrices based on the function values $f(\mathbf{x})$ at the desired stencils. Using the idea from the standard finite difference (FD) method, which approximates the derivative as a linear combination of the data values at the node points, we seek a set of weights w_j such that

$$\mathcal{L}f(\mathbf{x}_0) = \sum_{j=1}^n w_j f(\mathbf{x}_j), \quad (3)$$

where \mathcal{L} is a given linear operator. By approximating the function value $f(\mathbf{x})$ by the RBF interpolant $s(\mathbf{x})$, defined in equation (1), the corresponding weight vector $\mathbf{w} = (w_1, \dots, w_n)^T$ can be obtained by solving a linear system problem

$$\begin{bmatrix} \mathbf{A} \end{bmatrix} \begin{bmatrix} w_1 \\ w_2 \\ \vdots \\ w_n \end{bmatrix} = \begin{bmatrix} \mathcal{L}\phi(\|\mathbf{x} - \mathbf{x}_1\|)|_{\mathbf{x}=\mathbf{x}_0} \\ \mathcal{L}\phi(\|\mathbf{x} - \mathbf{x}_2\|)|_{\mathbf{x}=\mathbf{x}_0} \\ \vdots \\ \mathcal{L}\phi(\|\mathbf{x} - \mathbf{x}_n\|)|_{\mathbf{x}=\mathbf{x}_0} \end{bmatrix}. \quad (4)$$

This so-called RBF-FD method, a generalization of the FD method, does not require structured mesh and improves geometric flexibility significantly.

In this work, we use the Gaussian radial basis functions, i.e., $\phi(r) = e^{-\epsilon r^2}$. Here, ϵ is the shape parameter, which describes the flatness. The infinite smoothness of the Gaussian functions guarantees the basis functions are continuous in any derivatives. Furthermore, Fornberg and Flyer [11] showed that the interpolation matrix \mathbf{A} is always non-singular if Gaussian RBFs are used. In practice, however, the matrix \mathbf{A} can still be ill-conditioned when near-flat RBFs are used, i.e., $\epsilon \rightarrow 0$. To overcome this problem, the RBF-QR method proposed by Fornberg and Piret [1] is often used, which implements a basis conversion to improve the conditioning, described next.

B. RBF-QR method

The basic idea of the RBF-QR method is to expand the original Gaussian RBFs to a set of well-conditioned basis functions $\{V_i(\mathbf{x})\}_{i=1}^m$ with $m \geq n$, which spans the same function space. For general stencils, the new basis functions can be selected as combinations of polynomial powers, Chebyshev polynomials, and trigonometric functions [9]. In matrix notation, we have

$$\Phi(\mathbf{x}) = \begin{bmatrix} \phi(\|\mathbf{x} - \mathbf{x}_1\|) \\ \phi(\|\mathbf{x} - \mathbf{x}_2\|) \\ \vdots \\ \phi(\|\mathbf{x} - \mathbf{x}_n\|) \end{bmatrix} = \underbrace{\begin{bmatrix} c_1(\mathbf{x}_1) & \cdots & c_m(\mathbf{x}_1) \\ \vdots & & \vdots \\ c_1(\mathbf{x}_n) & \cdots & c_m(\mathbf{x}_n) \end{bmatrix}}_{\mathbf{C}} \underbrace{\begin{bmatrix} \epsilon^{\kappa_1} & & \\ & \ddots & \\ & & \epsilon^{\kappa_m} \end{bmatrix}}_{\mathbf{E}} \underbrace{\begin{bmatrix} V_1(\mathbf{x}) \\ V_2(\mathbf{x}) \\ \vdots \\ V_m(\mathbf{x}) \end{bmatrix}}_{\mathbf{V}(\mathbf{x})}, \quad (5)$$

where \mathbf{C} is a $O(1)$ coefficient matrix, and \mathbf{E} is a diagonal matrix with increasing powers of ϵ , i.e. $\kappa_1 \leq \dots \leq \kappa_m$. The QR-factorization of the coefficient matrix leads to $\mathbf{C} = \mathbf{Q}\mathbf{R}$, where \mathbf{Q} is unitary and \mathbf{R} is upper triangular. The new

basis functions are obtained as

$$\mathbf{\Psi}(\mathbf{x}) = \begin{bmatrix} \psi(\|\mathbf{x} - \mathbf{x}_1\|) \\ \psi(\|\mathbf{x} - \mathbf{x}_2\|) \\ \vdots \\ \psi(\|\mathbf{x} - \mathbf{x}_n\|) \end{bmatrix} = \mathbf{E}_n^{-1} \mathbf{Q}^* \mathbf{\Phi}(\mathbf{x}) = \mathbf{E}_n^{-1} \mathbf{R} \mathbf{E} \mathbf{V}(\mathbf{x}), \quad (6)$$

where \mathbf{E}_n^{-1} denotes the first $n \times n$ part of \mathbf{E} . Here, the matrix $\mathbf{E}_n^{-1} \mathbf{R} \mathbf{E}$ is upper triangular and well-conditioned. The main diagonal of this matrix only contains $O(1)$ elements. The new basis functions $\mathbf{\Psi}(\mathbf{x})$ improve the conditioning, and remain the same function space as the original RBFs set. The linear system problem shown in equation (4) can be written as

$$\underbrace{\begin{bmatrix} | & | & & | \\ \mathbf{\Psi}(\mathbf{x}_1) & \mathbf{\Psi}(\mathbf{x}_2) & \cdots & \mathbf{\Psi}(\mathbf{x}_n) \\ | & | & & | \end{bmatrix}}_{\mathbf{A}_\Psi} \begin{bmatrix} w_1 \\ w_2 \\ \vdots \\ w_n \end{bmatrix} = \begin{bmatrix} \mathcal{L}\psi(\|\mathbf{x} - \mathbf{x}_1\|)|_{\mathbf{x}=\mathbf{x}_0} \\ \mathcal{L}\psi(\|\mathbf{x} - \mathbf{x}_2\|)|_{\mathbf{x}=\mathbf{x}_0} \\ \vdots \\ \mathcal{L}\psi(\|\mathbf{x} - \mathbf{x}_n\|)|_{\mathbf{x}=\mathbf{x}_0} \end{bmatrix}. \quad (7)$$

The weight vector \mathbf{w} can then be calculated easily without inverting a nearly singular matrix. Readers are referred to Fornberg and Piret [1], Fornberg et al. [9] and Larsson et al. [10] for more details. The numerical implementation provided in Larsson et al. [10] is used in this work.

C. Global Jacobians

Assume the given domain are discretized by two different sets of scattered nodes, $\{\mathbf{x}_i^{(1)}\}_{i=1}^N$ and $\{\mathbf{x}_j^{(2)}\}_{j=1}^M$. We seek a set of differentiation matrices $\mathbf{D}_\mathcal{L}^{(\alpha,\beta)}$, which approximates the derivative $\mathcal{L}f(\mathbf{x}^{(\alpha)})$ based on the function values at node-set β as $\mathbf{D}_\mathcal{L}^{(\alpha,\beta)} f(\mathbf{x}^{(\beta)})$, for $\alpha, \beta = 1, 2$. For example, the differentiation matrix $\mathbf{D}_\mathcal{L}^{(2,1)}$ satisfies

$$\underbrace{\begin{bmatrix} w_{11} & w_{12} & \cdots & w_{1N} \\ w_{21} & w_{22} & \cdots & w_{2N} \\ \vdots & \vdots & & \vdots \\ w_{M1} & w_{M2} & \cdots & w_{MN} \end{bmatrix}}_{\mathbf{D}_\mathcal{L}^{(2,1)}} \begin{bmatrix} f(\mathbf{x}_1^{(1)}) \\ f(\mathbf{x}_2^{(1)}) \\ \vdots \\ f(\mathbf{x}_N^{(1)}) \end{bmatrix} = \begin{bmatrix} \mathcal{L}f(\mathbf{x}_1^{(2)}) \\ \mathcal{L}f(\mathbf{x}_2^{(2)}) \\ \vdots \\ \mathcal{L}f(\mathbf{x}_M^{(2)}) \end{bmatrix}. \quad (8)$$

For the j th row of the matrix $\mathbf{D}_\mathcal{L}^{(2,1)}$, $j = 1, 2, \dots, M$, we select the stencil for node $\mathbf{x}_j^{(2)}$ as the nearest $n \ll N$ nodes $\{\mathbf{x}_{i_1}^{(1)}, \mathbf{x}_{i_2}^{(1)}, \dots, \mathbf{x}_{i_n}^{(1)}\}$. The corresponding weights $w_{ji_1}, \dots, w_{ji_n}$ can then be obtained from equation (7), and the rest of the weights are set to be zero. The resulting assembled matrix, $\mathbf{D}_\mathcal{L}^{(2,1)}$, is sparse with $M \times n$ nonzero elements.

In this work, we implement the RBF-QR method to construct the global spatial derivatives for flow simulations. Discretization of the computational domain and the numerical scheme used for the evolution of incompressible flows are discussed in the following sections.

IV. Spatial Discretization

To avoid numerical instabilities in the flow simulations, we implement the RBF-QR method on an unstructured staggered grid, constructed using a single set of scattered nodes. We first discretize the computational domain Ω into M scattered nodes for the pressure component p using the Matlab algorithm `DistMesh` developed by Persson [26]. This algorithm generates unstructured triangular meshes in 2-D with the input distance function, which can be used for the desired local refinement. Inspired by the standard finite-volume methods, which define the flux across the cell boundaries, we arrange the velocity components on the cell edges. By collecting the midpoints of all edges of the triangular cells, we obtain a new set containing N scattered nodes for the horizontal and vertical velocity components, \mathbf{u} and \mathbf{v} in vector notation, respectively. This is different from the standard staggered grid, which evaluates the horizontal

and vertical velocities at different locations. By this construction, the ratio of the pressure grid to the velocity grid is around 1:3.

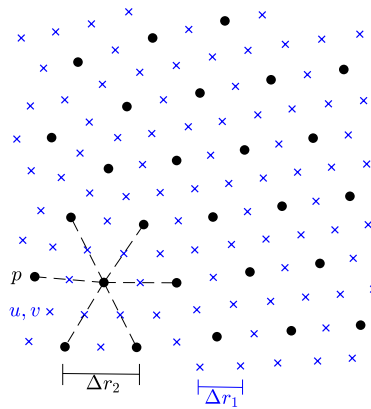


Fig. 1 Schematic of constructing the staggered grid: velocity grid (blue cross) and pressure grid (black dot).

Figure 1 shows the schematic of constructing the staggered grid. The characteristic length for each node-set, Δr , is determined as the locally averaged distance between the adjacent nodes. In the following, we use the notation $(\cdot)^{(1)}$ for the velocity grid and $(\cdot)^{(2)}$ for the pressure grid, respectively.

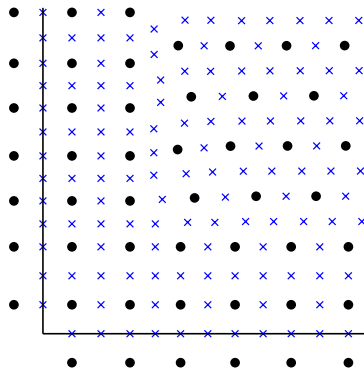


Fig. 2 Staggered grid near a corner.

To enforce the Neumann boundary condition on the wall, locally orthogonal grid near the boundary used in Shu et al. [28, 29] and a layer of ghost nodes are placed [30]. Identical to the arrangement for scattered nodes, the velocity grid is set at the midpoints of each adjacent pressure node pair. Figure 2 shows an example of the staggered grid near a corner. An SVD truncation with a threshold at 10^{-6} is used for the inversion of the interpolation matrix. This operation will only exclude orthogonal nodes to the derivative direction but not affect the scattered interior nodes. The transient flow simulations are obtained based on this staggered grid discretization, described next.

V. Numerical scheme

Start with the Navier-Stokes equations and the continuity equation,

$$\frac{\partial u}{\partial t} = - \left(u \frac{\partial u}{\partial x} + v \frac{\partial u}{\partial y} \right) - \frac{\partial p}{\partial x} + \frac{1}{\text{Re}} \left(\frac{\partial^2 u}{\partial x^2} + \frac{\partial^2 u}{\partial y^2} \right), \quad (9)$$

$$\frac{\partial v}{\partial t} = - \left(u \frac{\partial v}{\partial x} + v \frac{\partial v}{\partial y} \right) - \frac{\partial p}{\partial y} + \frac{1}{\text{Re}} \left(\frac{\partial^2 v}{\partial x^2} + \frac{\partial^2 v}{\partial y^2} \right), \quad (10)$$

$$\frac{\partial u}{\partial x} + \frac{\partial v}{\partial y} = 0. \quad (11)$$

which govern the motion of a general incompressible two-dimensional Newtonian fluid. All variables are nondimensionalized by the velocity scale V as well as length scale L , and Re denotes the Reynolds number. A variant of the fractional-step method used by Kim and Moin [31], a semi-implicit scheme, is employed to advance the incompressible flow in time. We propagate the flow field from j th time step to $(j+1)$ th time step by the following three-stage approach. The primitive variables u, v, p are expressed in the vector form $\mathbf{u}, \mathbf{v}, \mathbf{p}$, respectively.

- 1) We first use the second-order Adam-Bashforth method to discretize the nonlinear convective terms in time explicitly, which gives

$$\frac{\mathbf{u}^* - \mathbf{u}_j}{\Delta t} = \frac{3}{2} \mathbf{C}_j(\mathbf{u}_j) - \frac{1}{2} \mathbf{C}_{j-1}(\mathbf{u}_{j-1}), \quad (12)$$

$$\frac{\mathbf{v}^* - \mathbf{v}_j}{\Delta t} = \frac{3}{2} \mathbf{C}_j(\mathbf{v}_j) - \frac{1}{2} \mathbf{C}_{j-1}(\mathbf{v}_{j-1}), \quad (13)$$

where the functions \mathbf{C}_j is defined as

$$\mathbf{C}_j(\mathbf{q}) = - \left[\mathbf{u}_j \circ \left(\mathbf{D}_x^{(1,1)} \mathbf{q} \right) + \mathbf{v}_j \circ \left(\mathbf{D}_y^{(1,1)} \mathbf{q} \right) \right]. \quad (14)$$

Here, the quantity \mathbf{q} represents the input velocity components, \mathbf{u} or \mathbf{v} , and the symbol \circ denotes the Hadamard product.

- 2) In the second stage, the viscous terms are advanced by the second-order implicit Crank-Nicholson scheme in time as

$$\frac{\mathbf{u}^{**} - \mathbf{u}^*}{\Delta t} = \frac{1}{2\text{Re}} \mathbf{D}_\Delta^{(1,1)} (\mathbf{u}^* + \mathbf{u}^{**}), \quad (15)$$

$$\frac{\mathbf{v}^{**} - \mathbf{v}^*}{\Delta t} = \frac{1}{2\text{Re}} \mathbf{D}_\Delta^{(1,1)} (\mathbf{v}^* + \mathbf{v}^{**}), \quad (16)$$

which eliminates the time-step constraints imposed by viscosity. The use of Crank-Nicholson scheme also ensures that the fractional-step method still remains the overall accuracy at second-order in time.

- 3) In the third stage, we use the pressure correction to enforce incompressibility. We first calculate the divergence of velocity at the pressure grid as

$$\mathbf{F}_{j+1} = \mathbf{D}_x^{(2,1)} \mathbf{u}^{**} + \mathbf{D}_y^{(2,1)} \mathbf{v}^{**}. \quad (17)$$

Next, we determine the pressure correction as the solution of the Poisson's equation

$$\mathbf{D}_\Delta^{(2,2)} \mathbf{p}_{j+1} = \frac{1}{\Delta t} \mathbf{F}_{j+1}. \quad (18)$$

The velocity components at the $(j+1)$ th time step are then calculated as

$$\frac{\mathbf{u}_{j+1} - \mathbf{u}^{**}}{\Delta t} = -\mathbf{D}_x^{(1,2)} \mathbf{p}_{j+1}, \quad (19)$$

$$\frac{\mathbf{v}_{j+1} - \mathbf{v}^{**}}{\Delta t} = -\mathbf{D}_y^{(1,2)} \mathbf{p}_{j+1}. \quad (20)$$

Appropriate boundary conditions are prescribed in the integration process and are included in the differentiation matrices.

As stated above, four kinds of differentiation matrices are used to transfer the flow quantities between the staggered grid:

- 1) $\mathbf{D}_x^{(1,1)}$, $\mathbf{D}_y^{(1,1)}$, and $\mathbf{D}_\Delta^{(1,1)}$ with dimension $N \times N$ from velocity grid to velocity grid;
- 2) $\mathbf{D}_x^{(2,1)}$, $\mathbf{D}_y^{(2,1)}$ with dimension $M \times N$ from velocity grid to pressure grid;
- 3) $\mathbf{D}_\Delta^{(2,2)}$ with dimension $M \times M$ from pressure grid to pressure grid;
- 4) $\mathbf{D}_x^{(1,2)}$, $\mathbf{D}_y^{(1,2)}$ with dimension $N \times M$ from pressure grid to velocity grid.

To approximate these spatial derivatives with the lowest truncation error, we propose a rigorous error analysis to obtain the optimal combination of the shape parameter, ϵ , and the stencil size, n , discussed next.

VI. Error analysis

We start with the modified wavenumber analysis, which is commonly used to measure the accuracy of different numerical schemes, see Moin [23]. For a given finite difference scheme, the modified wavenumber, k^* , is derived by the discrete differentiation of a sinusoidal function $g(x) = e^{ikx}$. Given the grid spacing Δx , the comparison between $k^*\Delta x$ and $k\Delta x$ shows how well a finite difference scheme behaves at different wavenumbers. In the following, we adapt this analysis for scattered nodes to gauge the accuracy of the RBF-QR method. Prior to performing the modified wavenumber analysis, we identify the optimal parameters using a fixed nondimensionalized wavenumber, $k\Delta r = 1$. The test function takes the form

$$g(x) = \cos\left(\frac{x}{\Delta r_\eta}\right) \cos\left(\frac{y}{\Delta r_\eta}\right), \quad (21)$$

where η is the index of the base grid. The corresponding wavelength is $\lambda = 2\pi\Delta r_\eta$. The relative error of the RBF-QR method is determined in an average form as

$$e^{(\alpha,\beta)} = \frac{1}{N} \sum_{j=1}^N \frac{|\delta_j^{(\alpha,\beta)} g(\mathbf{x}^{(\beta)}) - \mathcal{L}g(\mathbf{x}^{(\alpha)})|}{\max\{|\mathcal{L}g(\mathbf{x})|\}}, \quad (22)$$

where δ_j represents the local RBF differentiation operation at the j th node. The best approximations are then found as the local minima of the error by varying the nondimensionalized shape parameter, $\epsilon\Delta r$, and the stencil size, n . Later we will show that the accuracy of the obtained optimal differentiation matrices is comparable to the 4th-order Padé scheme, which is well-suited for direct numerical simulations. The use of the nondimensionalized shape parameter as parameterization is discussed in Appendix.

The stencils used for the RBF-QR method are selected as the nearest n nodes. Figure 3 shows the examples of stencils used for the four different cases. A randomly generated mesh consisting of nodes with constant spacing is used for the error calculation.

A. Velocity grid

We first look at the differentiation matrices $\mathbf{D}^{(1,1)}$, which corresponds to case (a) in figure 3. Figure 4 shows the relative error contour for different parameters. As the local stencil is not homogeneous in the x and y directions, the resulting error contour plots are different for x and y derivatives, as expected. Despite the inhomogeneity of the mesh, we find that the same stencil size, $n = 15$, is optimal for the first derivatives in both the x and y directions. This result indicates that this stencil size may be optimal for first derivatives in arbitrary directions, which can always be expressed in terms of x and y derivatives. We will show later this conjecture also holds for $\mathbf{D}^{(2,1)}$, $\mathbf{D}^{(2,2)}$ and $\mathbf{D}^{(1,2)}$. This finding is encouraging since the local topology of an unstructured mesh, in principle, can have arbitrary orientations. Similarly, the same optimal nondimensionalized shape parameter, $\epsilon\Delta r_1 = 0.38$, is also found for the first derivatives. However, this no longer holds for the pressure grid. For the Laplace differentiation matrix, $\mathbf{D}_\Delta^{(1,1)}$, figure 4(c) shows that the optimal shape parameter is largely independent of the stencil size. Although the local minimum is achieved at $n = 27$, a smaller stencil size, e.g., $n = 23$, can also be used in the computation without losing much accuracy.

We further perform the modified wavenumber analysis for the optimal differentiation matrices to gauge the truncation error at different wavenumbers. The modified wavenumbers are calculated as

$$k^* = \frac{1}{N} \sum_{j=1}^N -i \left(\delta_x e^{ikx} \right) \circ e^{-ikx} \quad \text{for } x \text{ derivatives,} \quad \text{or} \quad k^* = \frac{1}{N} \sum_{j=1}^N -i \left(\delta_y e^{iky} \right) \circ e^{-iky} \quad \text{for } y \text{ derivatives,} \quad (23)$$

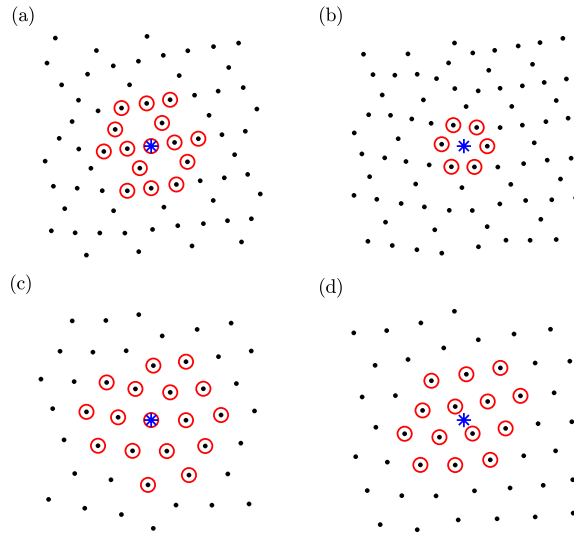


Fig. 3 Stencils (red circles) used to obtain the differentiation matrices (a) $D^{(1,1)}$ with $n = 15$; (b) $D^{(2,1)}$ with $n = 6$; (c) $D^{(2,2)}$ with $n = 17$; (d) $D^{(1,2)}$ with $n = 14$ at the given nodes (blue stars).

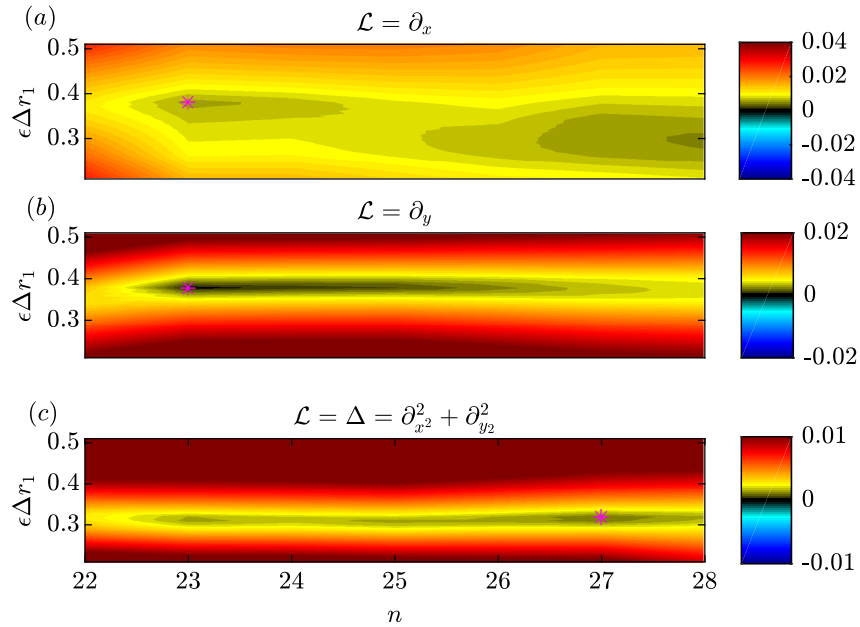


Fig. 4 Relative error contours for: (a) $D_x^{(1,1)}$; (b) $D_y^{(1,1)}$; (c) $D_\Delta^{(1,1)}$. The local minima are marked as magenta stars. The combination $(n, \epsilon\Delta r_1) = (15, 0.38)$ is optimal for the first derivatives, and $(n, \epsilon\Delta r_1) = (27, 0.32)$ is optimal for the Laplacian.

where the exponential function is evaluated element-by-element. Figure 5 displays the modified wavenumber diagrams for the optimal differentiation matrices, $D^{(1,1)}$. Results for the 4th and 6th Padé-type methods are shown as comparisons.

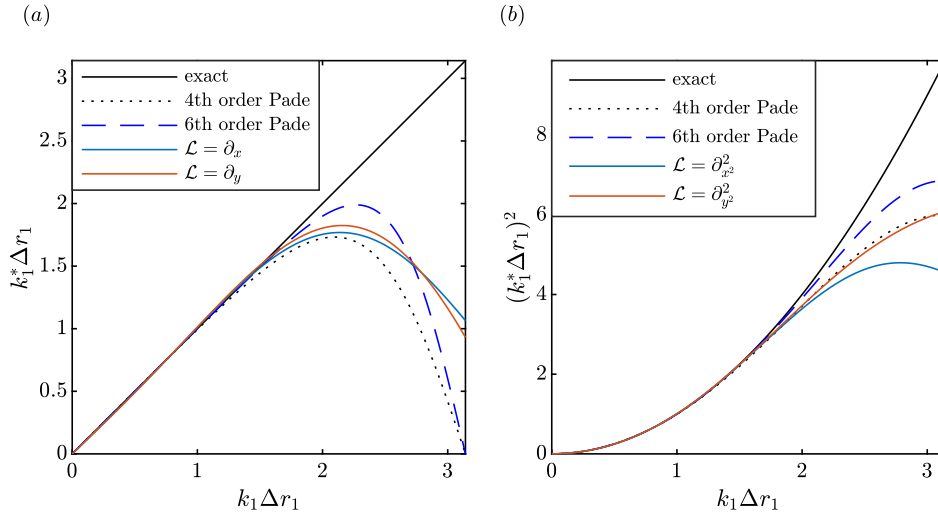


Fig. 5 Modified wavenumber diagrams for the optimal differentiation matrices $D^{(1,1)}$. The operator \mathcal{L} takes the form of (a) first-order and (b) second-order derivatives. Results for Padé-type methods are shown as comparisons.

For the first derivatives, figure 5(a) shows that the the optimal differentiation matrices, $D_x^{(1,1)}$ and $D_y^{(1,1)}$, provide accuracy better than the 4th-order Padé scheme. For the second derivatives in the y direction, the optimal differentiation matrix performs almost identical to the 4th-order Padé-type scheme. In the x direction, the accuracy is still comparable to the 4th-order Padé scheme up to $k \Delta r = 2$.

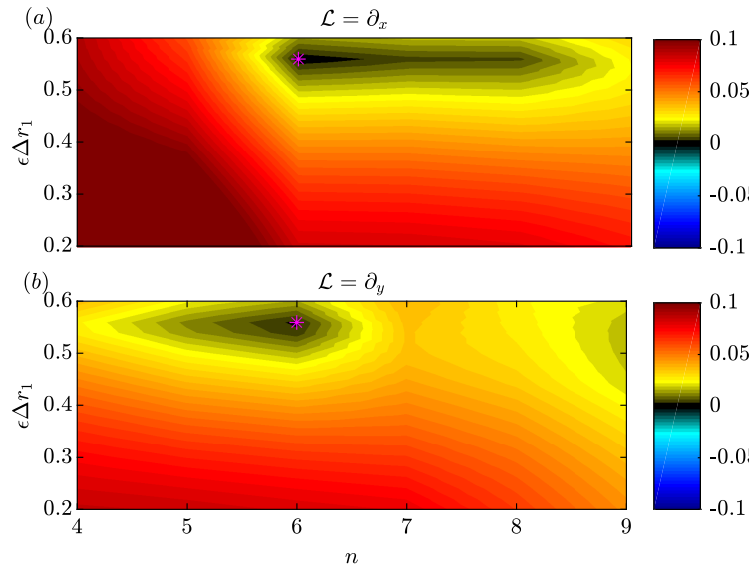


Fig. 6 Relative error contours for: (a) $D_x^{(2,1)}$; (b) $D_y^{(2,1)}$. The local minima are marked as magenta stars. The combination $(n, \epsilon \Delta r_1) = (6, 0.56)$ is optimal for both cases.

We then move to case (b) in figure 3, which is used to compute the divergence of velocity on the pressure grid. In this case, we are focusing on the error of the RBF-QR method when approximating the first-order derivatives, shown in figure 6. It can be seen that the combination $(n, \epsilon \Delta r_1) = (6, 0.56)$ is optimal for both the x and y derivatives. This

stencil size corresponds to the first layer of surrounding velocity nodes; see figure 3(b). As discussed above, this optimal combination can then be used to approximate the derivatives in arbitrary directions.

B. Pressure grid

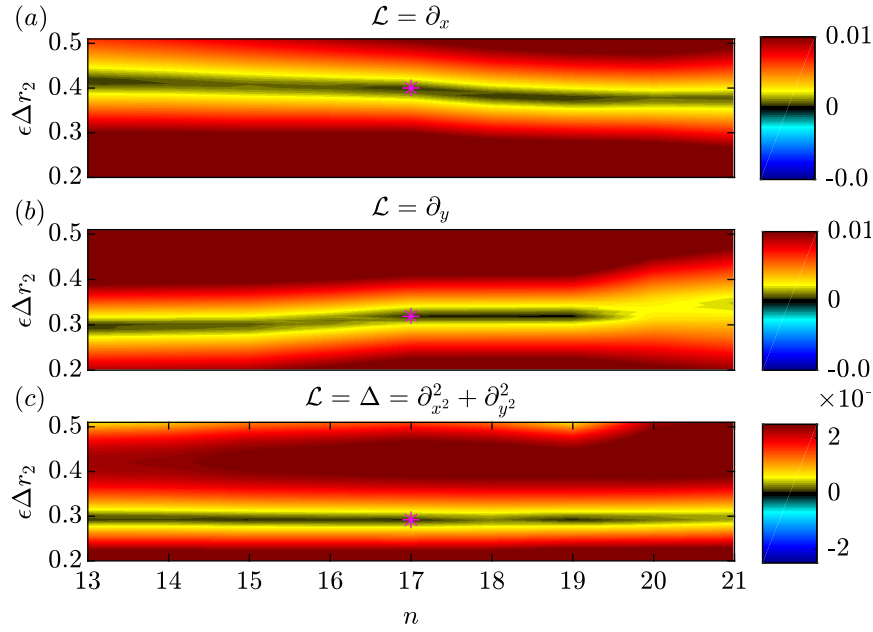


Fig. 7 Relative error contours for: (a) $D_x^{(2,2)}$; (b) $D_y^{(2,2)}$; (c) $D_\Delta^{(2,2)}$. The local minima are marked as magenta stars. The stencil size $n = 17$ is optimal for all the three cases.

Next, we perform the error analysis for the differentiation matrices $\mathbf{D}^{(2,2)}$, which correspond to case (b) in figure 3. In this case, the same optimal stencil size, $n = 17$, is found for both first and second derivatives. For the Laplace operator, it can be seen from figure 7(c) that the relative error is generally invariant with the stencil size. Similar to case (c) in the figure, a constant nondimensionalized shape parameter, $\epsilon\Delta r_2 = 0.29$, is optimal for the pressure grid.

Figure 8 shows the modified wavenumber diagrams for the differentiation matrices $\mathbf{D}^{(2,2)}$. Results for the 4th and 6th-order Padé-type methods are shown for comparison. For the first-order derivatives, figure 8(a) shows that the obtained accuracy is comparable to the 6th-order Padé scheme up to $k_2\Delta r_2 = 1.5$ in the x direction and the 4th-order Padé scheme up to $k_2\Delta r_2 = 2$ in the y direction, respectively. Note that only the optimal second-order differentiation matrix, $\mathbf{D}_\Delta^{(2,2)}$, will be used when solving the pressure Poisson equation in the computation. We can see from figure 8(b) that the accuracy of such a spatial discretization is almost the same as the 6th-order Padé scheme.

Figure 9 shows the error for case (d) in figure 3, which is used to enforce the incompressibility condition from the pressure correction. The error contours for the first-order x and y derivatives are similar in this case, and the same optimal combination, $(n, \epsilon\Delta r_1) = (14, 0.38)$, is found. Compared to figure 3(b), more surrounding nodes are required to minimize the error in this case.

VII. Lid-Driven cavity flows

We study the internal flow of a lid-driven cavity to demonstrate the behavior of the proposed scheme shown in §V and the optimal differentiation matrices obtained in §VI. Consider the flow inside a unit square cavity Ω driven by the motion of the top wall with unit velocity. No-slip boundary conditions are prescribed at wall boundaries. The normal derivative of the pressure is set to be zero at all boundaries. The time-marching calculations are started with the flow at rest everywhere in the computational domain except at the top wall.

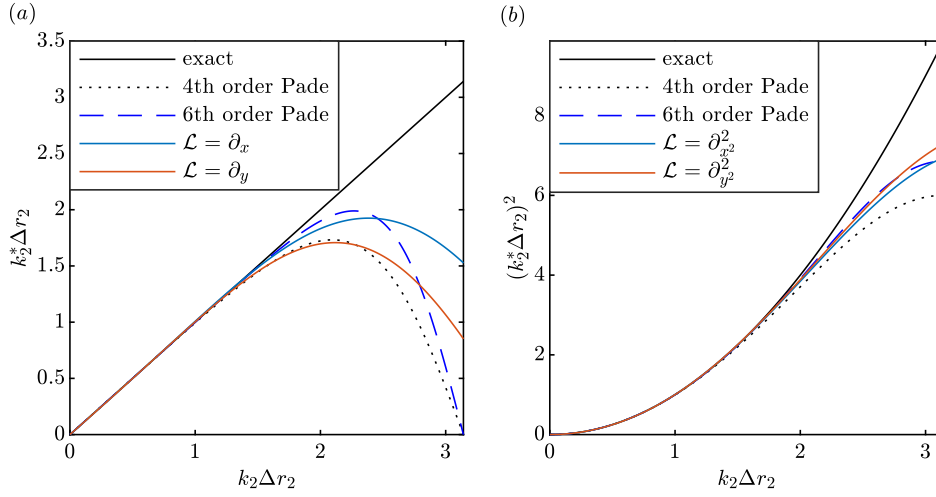


Fig. 8 Modified wavenumber diagrams for the differentiation matrices $D^{(2,2)}$ with the optimal combination (n, ϵ) . The operator \mathcal{L} takes the form of (a) first-order and (b) second-order derivatives. Results for Padé-type methods are shown as comparisons.

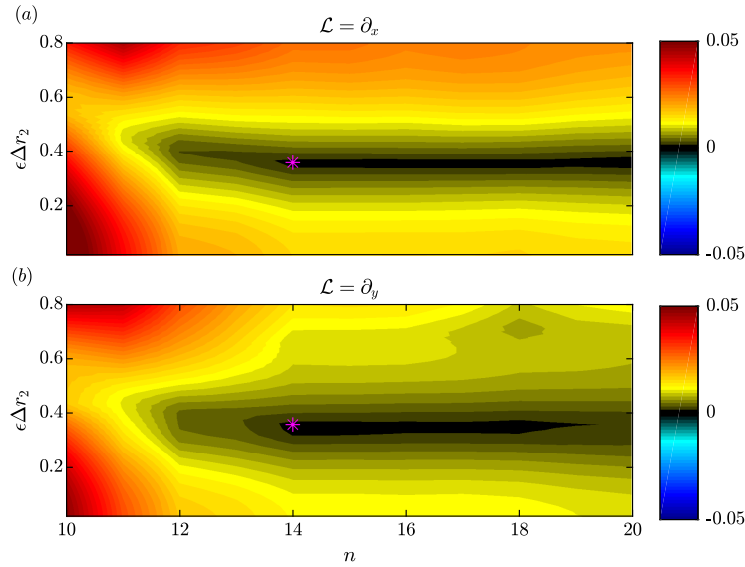


Fig. 9 Relative error contours for: (a) $D_x^{(1,2)}$; (b) $D_y^{(1,2)}$. The local minima are marked as magenta stars. The combination $(n, \epsilon \Delta r_1) = (14, 0.38)$ is optimal for both cases.

Figure 10 shows the discretization of the unit square cavity $\Omega = [0, 1] \times [0, 1]$ with $N = 13491 \approx 116^2$ and $M = 4677 \approx 68^2$. The characteristic lengths for the two node-sets are $\Delta r_1 = 0.008$ and $\Delta r_2 = 0.016$, respectively. A time step $\Delta t = 0.005$, corresponding to CFL number at 0.625, is used in the computation. Results at Reynolds numbers ranging from 100 to 3200 are investigated for comparison with the classical results by Ghia et al. [27]. Stable solutions are obtained without implementing hyperviscosity approaches.

Figure 11 shows the obtained steady-state velocity profiles through the horizontal and vertical centerlines of the cavity. Compared to the benchmark data provided by Ghia et al. [27] using 129^2 nodes, good agreements are found at different Reynolds numbers. This result implies that the optimal differential matrices provide good performance in the

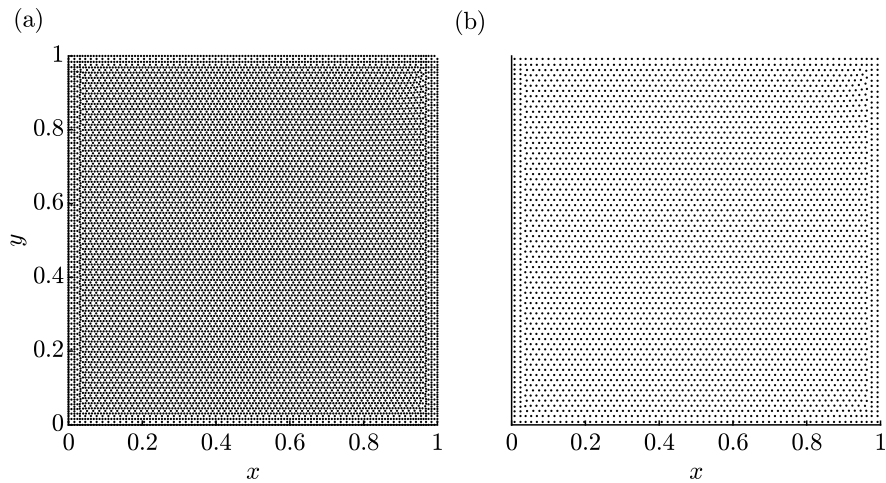


Fig. 10 Computational grids in a unit square cavity: (a) velocity grid with $N = 13491 \approx 116^2$ nodes; (b) pressure grid with $M = 4677 \approx 68^2$ nodes.

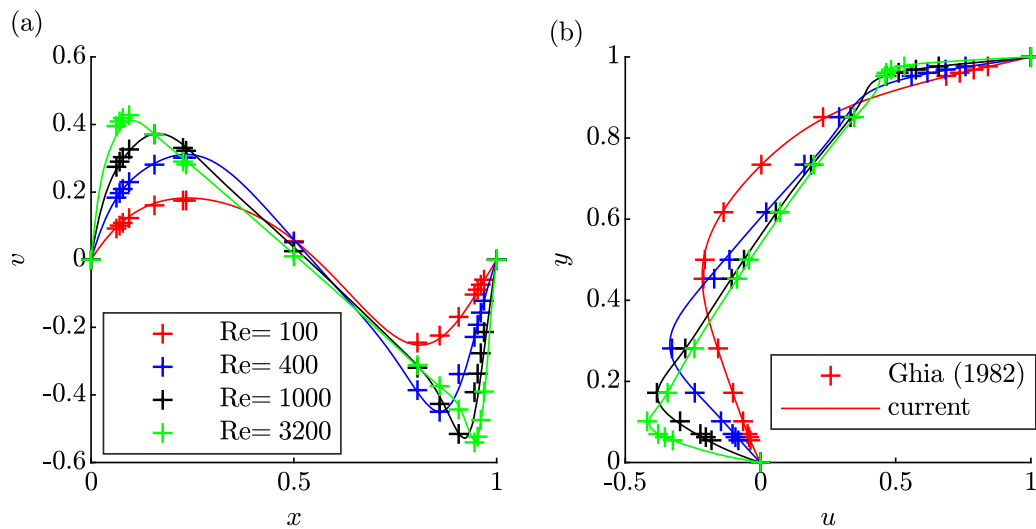


Fig. 11 Velocity profiles at $Re = 100$ (red), $Re = 400$ (blue), $Re = 1000$ (black) and $Re = 3200$ (green) through the: (a) horizontal centerline; (b) vertical centerline. The results obtained using the proposed scheme (solid) are compared to Ghia et al. [27] ('+').

simulation of two-dimensional incompressible flows.

To further validate that the proposed scheme can be utilized as a transient solver, we visualize the flow field at different times in figure 12. It can be seen that stable solutions and highly-resolved flow patterns are obtained in the

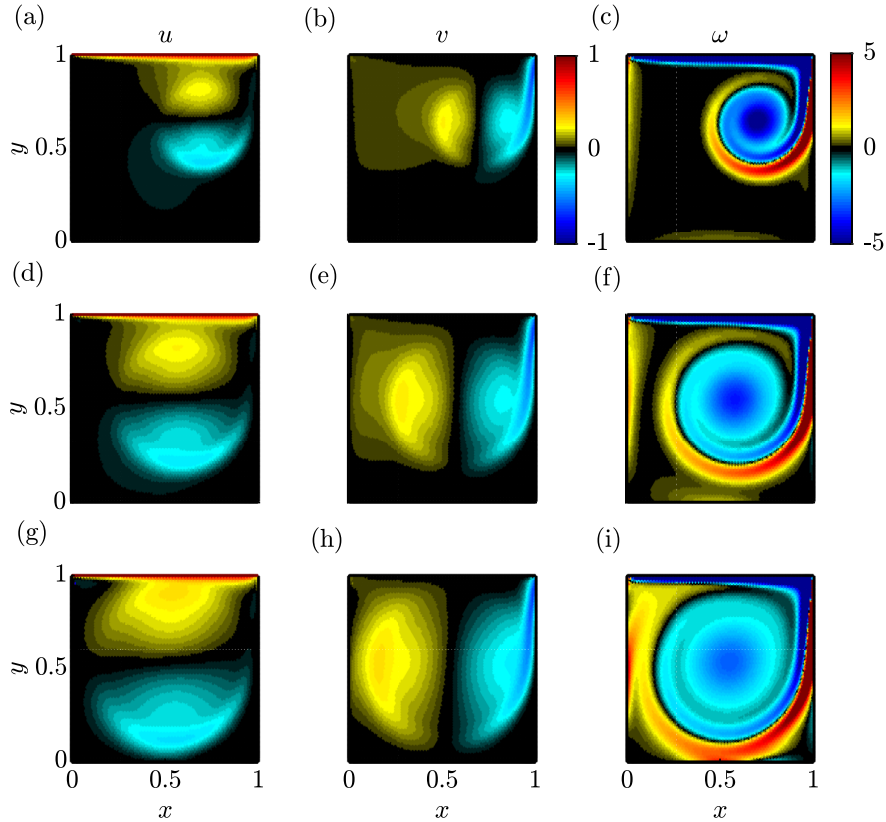


Fig. 12 Transient horizontal velocity (left column), vertical velocity (middle column) and vorticity (right column) for $Re = 3200$ at: (a-c) $t = 7.5$; (d-f) $t = 15$; (g-i) $t = 22.5$. The vorticity vector is calculated as $\omega = D_x^{(1,1)}v - D_y^{(1,1)}u$.

computational process. The vorticity, $\omega = \partial v / \partial x - \partial u / \partial y$, is displayed in the right column of figure 12, and the generation of the primary vortex can be observed. This result confirms that this scheme is well-suited for simulating the unsteady incompressible flows.

VIII. Conclusions

In this work, we introduce a means of error analysis to identify the optimal parameters for the RBF-QR discretizations. We propose an RBF-QR-based fractional-step method for the unsteady incompressible Navier-Stokes equations that utilize the optimal discretizations. To achieve numerical stability, we construct an unstructured staggered grid that assigns the velocities at the middle of cell edges and pressure at the cell vertices. We perform the wavenumber analysis to gauge the accuracy of the optimal RBF-QR discretizations, and the results are comparable with the 4th-order Padé scheme. We demonstrate the use of the proposed scheme and optimal parameters by studying the lid-driven cavity problem at different Reynolds numbers. The obtained results are compared to Ghia et al. [27], and good agreements are found for all cases. The long-term goal of this work is to use the optimal RBF-based differentiation matrices for hydrodynamic stability analyses in complex geometries.

Acknowledgments

We would like to thank Bengt Fornberg for sharing his insights into RBF discretizations. We gratefully acknowledge support by the National Science Foundation under Grant No. CBET-1953999 (PM Ron Joslin).

Appendix: nondimensionalized shape parameter

In the following, we will motivate the use of $\epsilon\Delta r$ as an appropriate parameterization of the optimization problem. Consider a given location \mathbf{x}_0 and the associated neighborhood $\{\mathbf{x}_j\}_{j=1}^n$, which is characterized by the distance Δr . A scaled node-set $\{\tilde{\mathbf{x}}_j\}_{j=1}^n$ with unit characteristic distance can be obtained under the linear transformation

$$\tilde{\mathbf{x}} = \frac{1}{\Delta r}\mathbf{x} + d, \quad (\text{A.1})$$

where the entire topology is scaled by $1/\Delta r$, and d is a constant translation. The relative topology between each node remains the same under this transformation. The form of the radial function ϕ allows one to write

$$\tilde{\phi}(\epsilon r) \equiv \phi(r; \epsilon). \quad (\text{A.2})$$

We can then write

$$\phi(\|\mathbf{x}_i - \mathbf{x}_j\|; \epsilon) = \tilde{\phi}(\epsilon\|\mathbf{x}_i - \mathbf{x}_j\|) = \phi(\|\tilde{\mathbf{x}}_i - \tilde{\mathbf{x}}_j\|; \epsilon\Delta r). \quad (\text{A.3})$$

Therefore, the radial function for the scaled node-set is described by the nondimensionalized shape parameter, $\epsilon\Delta r$. The corresponding interpolation matrix \mathbf{A} , defined in equation (2), is then a function of the nondimensionalized shape parameter only. So as the nondimensionalized weight vector $\tilde{\mathbf{w}} \equiv (\Delta r)^q \mathbf{w} = \mathbf{A}^{-1} \tilde{\mathcal{L}} \Phi(\mathbf{x}_0)$, where $\tilde{\mathcal{L}} = ((\Delta r)^q \mathcal{L})$ and q is the order of the derivative. We seek the optimal parameters which minimize the relative error

$$E_0 = \frac{|\sum_{j=1}^n w_j g(k\mathbf{x}_j; \Delta r) - \mathcal{L}g(k\mathbf{x}_0; \Delta r)|}{\max\{|\mathcal{L}g(k\mathbf{x}; \Delta r)|\}}. \quad (\text{A.4})$$

Here, $g(k\mathbf{x}; \Delta r)$ is a sinusoidal function, where k is the characteristic wavenumber and $\gamma = k\Delta r$ is a constant. The error can then be written as

$$E_0 = \tilde{E}_0 = \frac{|\sum_{j=1}^n \tilde{w}_j g(\gamma\tilde{\mathbf{x}}_j; 1) - \tilde{\mathcal{L}}g(\gamma\tilde{\mathbf{x}}_0; 1)|}{\max\{|\tilde{\mathcal{L}}g(\gamma\tilde{\mathbf{x}}; 1)|\}}, \quad (\text{A.5})$$

where \tilde{E}_0 represents the error for the scaled node-set. It can be seen that the error only depends on the stencil size, n , and the nondimensionalized shape parameter, $\epsilon\Delta r$. The optimization problem then becomes determining the nondimensionalized parameters that provide the best accuracy for the scaled node-set. The the optimal combination $(n, \epsilon\Delta r)$ is therefore invariant if the local relative topology is fixed.

References

- [1] Fornberg, B., and Piret, C., "A stable algorithm for flat radial basis functions on a sphere," *SIAM J. Sci. Comput.*, Vol. 30, No. 1, 2008, pp. 60–80.
- [2] Hardy, R. L., "Multiquadric equations of topography and other irregular surfaces," *J. Geophys. Res.*, Vol. 76, No. 8, 1971, pp. 1905–1915.
- [3] Powell, M. J., "The theory of radial basis function approximation in 1990," *Adv. Numer. Anal.*, 1992, pp. 105–210.
- [4] Larsson, E., and Fornberg, B., "Theoretical and computational aspects of multivariate interpolation with increasingly flat radial basis functions," *Comput. Math. Appl.*, Vol. 49, No. 1, 2005, pp. 103–130.
- [5] Tolstykh, A. I., "On using RBF-based differencing formulas for unstructured and mixed structured-unstructured grid calculations," *Proceedings of the 16th IMACS world congress*, Vol. 228, Lausanne, 2000, pp. 4606–4624.
- [6] Flyer, N., and Wright, G. B., "A radial basis function method for the shallow water equations on a sphere," *Proc. Math. Phys. Eng. Sci.*, Vol. 465, No. 2106, 2009, pp. 1949–1976.
- [7] Flyer, N., Lehto, E., Blaise, S., Wright, G. B., and St-Cyr, A., "A guide to RBF-generated finite differences for nonlinear transport: Shallow water simulations on a sphere," *J. Comput. Phys.*, Vol. 231, No. 11, 2012, pp. 4078–4095.
- [8] Fornberg, B., and Lehto, E., "Stabilization of RBF-generated finite difference methods for convective PDEs," *J. Comput. Phys.*, Vol. 230, No. 6, 2011, pp. 2270–2285.

- [9] Fornberg, B., Larsson, E., and Flyer, N., “Stable computations with Gaussian radial basis functions,” *SIAM J. Sci. Comput.*, Vol. 33, No. 2, 2011, pp. 869–892.
- [10] Larsson, E., Lehto, E., Heryudono, A., and Fornberg, B., “Stable computation of differentiation matrices and scattered node stencils based on Gaussian radial basis functions,” *SIAM J. Sci. Comput.*, Vol. 35, No. 4, 2013, pp. A2096–A2119.
- [11] Fornberg, B., and Flyer, N., “Solving PDEs with radial basis functions,” *Acta Numer.*, Vol. 24, 2015, p. 215.
- [12] Despotis, G., and Tsangaris, S., “Fractional step method for solution of incompressible Navier-Stokes equations on unstructured triangular meshes,” *Internat. J. Numer. Methods Fluids*, Vol. 20, No. 11, 1995, pp. 1273–1288.
- [13] Hwang, Y.-H., “Calculations of incompressible flow on a staggered triangular grid, part II: applications,” *Numer. Heat Transf.*, Vol. 27, No. 3, 1995, pp. 337–353.
- [14] Hwang, Y.-H., “Calculations of incompressible flow on a staggered triangular grid, part I: mathematical formulation,” *Numer. Heat Transf.*, Vol. 27, No. 3, 1995, pp. 323–336.
- [15] Rida, S., McKenty, F., Meng, F., and Reggio, M., “A staggered control volume scheme for unstructured triangular grids,” *Internat. J. Numer. Methods Fluids*, Vol. 25, No. 6, 1997, pp. 697–717.
- [16] Thomadakis, M., and Leschziner, M., “A pressure-correction method for the solution of incompressible viscous flows on unstructured grids,” *Internat. J. Numer. Methods Fluids*, Vol. 22, No. 7, 1996, pp. 581–601.
- [17] Shu, H., Xu, M., Duan, X., Li, Y., Sun, Y., Li, R., and Ding, P., “A staggered grid method for solving incompressible flow on unstructured meshes,” *Comput. Model. Eng. Sci.*, Vol. 123, No. 2, 2020, pp. 509–523.
- [18] Franke, R., “Scattered data interpolation: tests of some methods,” *Math. Comp.*, Vol. 38, No. 157, 1982, pp. 181–200.
- [19] Carlson, R. E., and Foley, T. A., “The parameter R2 in multiquadric interpolation,” *Comput. Math. Appl.*, Vol. 21, No. 9, 1991, pp. 29–42.
- [20] Rippa, S., “An algorithm for selecting a good value for the parameter c in radial basis function interpolation,” *Adv. Comput. Math.*, Vol. 11, No. 2, 1999, pp. 193–210.
- [21] Fornberg, B., and Wright, G., “Stable computation of multiquadric interpolants for all values of the shape parameter,” *Comput. Math. Appl.*, Vol. 48, No. 5-6, 2004, pp. 853–867.
- [22] Fasshauer, G. E., and Zhang, J. G., “On choosing “optimal” shape parameters for RBF approximation,” *Numer. Algorithms*, Vol. 45, No. 1-4, 2007, pp. 345–368.
- [23] Moin, P., *Fundamentals of engineering numerical analysis*, Cambridge University Press, 2010.
- [24] Park, N., and Mahesh, K., “Numerical and modeling issues in LES of compressible turbulence on unstructured grids,” *45th AIAA Aerospace Sciences Meeting and Exhibit*, 2007, p. 722.
- [25] Nishikawa, H., “A flexible gradient method for unstructured-grid solvers,” *Internat. J. Numer. Methods Fluids*, Vol. 93, No. 6, 2021, pp. 2015–2021.
- [26] Persson, P.-O., “Mesh generation for implicit geometries,” Ph.D. thesis, Massachusetts Institute of Technology, 2005.
- [27] Ghia, U., Ghia, K. N., and Shin, C., “High-Re solutions for incompressible flow using the Navier-Stokes equations and a multigrid method,” *J. Comput. Phys.*, Vol. 48, No. 3, 1982, pp. 387–411.
- [28] Shu, C., Ding, H., and Yeo, K., “Local radial basis function-based differential quadrature method and its application to solve two-dimensional incompressible Navier–Stokes equations,” *Comput. Methods Appl. Mech. Engrg.*, Vol. 192, No. 7-8, 2003, pp. 941–954.
- [29] Shu, C., Ding, H., and Yeo, K., “Computation of incompressible Navier-Stokes equations by local RBF-based differential quadrature method,” *CMES Comput. Model. Eng. Sci.*, Vol. 7, No. 2, 2005, pp. 195–206.
- [30] Chinchapatnam, P. P., Djidjeli, K., Nair, P., and Tan, M., “A compact RBF-FD based meshless method for the incompressible Navier—Stokes equations,” *Proc. IME. M-J Eng. Marit. Environ.*, Vol. 223, No. 3, 2009, pp. 275–290.
- [31] Kim, J., and Moin, P., “Application of a fractional-step method to incompressible Navier-Stokes equations,” *J. Comput. Phys.*, Vol. 59, No. 2, 1985, pp. 308–323.